Materials Today Communications 35 (2023) 105870

Contents lists available at ScienceDirect

Materials Today Communications

journal homepage: www.elsevier.com/locate/mtcomm

Microstructure and texture characterisation of friction stir welded CoCrNi and CoCrFeMnNi multi-principle element alloys

Ricardo Henrique Buzolin [a,b,*], Tim Richter [c], Florian Pixner [b,d], Michael Rhode [c,e], Dirk Schroepfer [c], Norbert Enzinger [b]

[a] Christian Doppler Laboratory for Design of High-Performance Alloys by Thermomechanical Processing, Kopernikusgasse 24/I, 8010 Graz, Austria
[b] Institute of Materials Science, Joining and Forming at Graz University of Technology, Kopernikusgasse 24/I, 8010 Graz, Austria
[c] Bundesanstalt für Materialforschung und -prüfung (BAM), Department 9 Component Safety, Unter Den Eichen 87, 12205 Berlin, Germany
[d] LKR Light Metals Technologies, Austrian Institute of Technology, Lamprechtshausenerstraße 61, 5282 Ranshofen, Austria
[e] Otto-von-Guericke Universität, Institute for Materials Science and Joining Technology, Universitätsplatz 2, 39106 Magdeburg, Germany

ARTICLE INFO

Keywords:
Multi-principal element alloys
Friction stir welding
High entropy alloy
Medium entropy alloy
Microstructure
Electron backscattered diffraction
Crystallographic texture

ABSTRACT

This work investigates the microstructure formed in friction stir welds of FCC alloys, focused on two multi-principal alloys: a CoCrFeMnNi high-entropy alloy (HEA) and a CoCrNi medium-entropy alloy (MEA). A commercial stainless steel AISI 304 is used for comparison. The largest nugget was formed in the MEA, while the smallest was formed in the HEA. Grain refinement occurs in the stirred zone in all welds. Discontinuous dynamic recrystallisation is the predominant restoration mechanism during friction stir welding of the three investigated alloys. A sharp decrement in the Σ3 boundary fraction occurs in the stirred zone of the AISI 304 and HEA welds, while comparable values with the base metal are found for the MEA weld. The peak in the maximum index of crystallographic texture is observed on the advancing side of the stirred zone of the AISI 304 weld. A strong $<001>$ θ-fibre texture is formed in the advancing side of the nugget in the AISI 304 from a well-established $\{123\}<634>$ S-type texture in the base metal. Multiple crystallographic texture components without specific fibres are identified in most regions of the welds, indicating the complex shear path history during friction stir welding.

1. Introduction

Multi-principal elemental alloys, known as medium and high entropy alloys (MEA and HEA, respectively), started being explored in the early 2000s, and many researchers investigated their properties [1–4]. Since they are alloys composed of three or more elements forming simple solid solution phases [5,6], theoretically, infinite combinations of chemical elements and compositions can produce a multi-principal elemental alloy. Therefore, some works attempted to characterise multi-principal alloys in terms of crystal structure and present chemical elements [7], and others proposed to classify alloys in terms of their operative strengthening mechanisms [2]. These alloys have been investigated due to their promising properties, either for structural applications, such as high fracture resistance for cryogenic applications [8], high compressive strength [9], and a high strength-ductility ratio [10] or as functional materials, such as catalytical [11,12] or magnetic materials [13–15] and coatings for high-temperature or high oxidation resistance [16,17], among others. Of the various MEA and HEAs, the

Abbreviations: AS, advancing side; BM, base metal; BSE, backscattered electrons; CDRX, continuous dynamic recrystallisation; CSL, coincident site lattice; DDRX, discontinuous dynamic recrystallisation; DRV, dynamic recovery; EBSD, electron backscattered diffraction; EDX, energy-dispersive X-ray spectroscopy; EMPA, electron microprobe analysis; f_{HAGB}, fraction of high angle grain boundaries; f_{LAGB}, fraction of low angle grain boundaries; $f_{\Sigma 3}$, fraction of Σ3 boundaries; GND, geometric necessary dislocations; GOS, grain orientation spread; FCC, face-centred cubic; FSP, friction stir processing; FSW, friction stir welding; HAZ, heat-affected zone; HEA, high entropy alloy; KAM, kernel average misorientation; LAGB, low-angle grain boundary; LW, laser welding; MEA, medium entropy alloy; OES, optical emission spectroscopy; PF, pole figure; RS, retreating side; SEM, scanning electron microscopy; SZ, stirred zone; TMAZ, thermomechanical affected zone; Φ, grain size.

* Corresponding author at: Christian Doppler Laboratory for Design of High-Performance Alloys by Thermomechanical Processing, Kopernikusgasse 24/I, 8010 Graz, Austria.
E-mail address: ricardo.buzolin@tugraz.at (R.H. Buzolin).

https://doi.org/10.1016/j.mtcomm.2023.105870
Received 15 March 2023; Accepted 21 March 2023
Available online 29 March 2023

ones containing 3d-transitional metallic elements with FCC crystal structure showed outstanding toughness and ductility, especially at cryogenic and low temperatures [2,18]. Among those alloys, single-phase FCC CoCrNi MEA [19] and CoCrFeMnNi HEA [20] have been investigated in detail in other works.

Material processing is inevitable for engineering applications and joining is often required. There is currently a specific basis for the effects of welding processes on multi-principal elemental alloys [21]. Among the welding techniques, friction stir welding (FSW) is a solid-state process with many advantages compared to conventional fusion welding processes [22]. It can suppress defects, such as blow holes, porosity, cracking and segregation, which often occur in fusion welds [23,24] since the maximum temperature during FSW is consistently below the macroscopic melting temperature of the processed material. In addition, good properties in the stir zone (SZ), e.g., high mechanical strength and fracture elongation, are reported due to grain refinement [25–27]. Regarding the studies on FSW of muti-principal alloys, the works are primarily focused on the correlation between the formed microstructure with the mechanical properties.

Regarding the single-phase FCC multi-element alloys, considerable grain refinement and increment in strength are shown for an FSW welded CoCrNi [28] MEA. The size of recrystallised grains in the SZ of an FSW welded single-phase FCC CoCrFeNi HEA increased with the increased rotation speed of the welding tool [29]. In addition, inhomogeneities in grain size and composition occurred, forming onion-ring or fishbone structures in the SZ. The tensile properties of the FSW welded joints of single-phase FCC CoCrFeNi were strongly affected by the grain size in the SZ, mainly controlled by the heat input during the FSW process [29].

The microstructure and tensile strength of FSW welds of the CrMnFeCoNi HEA were investigated, and slightly higher strength was achieved if the welds were rapidly cooled [30]. The mechanical properties of a double-side butt welded CoCrFeMnNi HEA doped with C were investigated. The increase in strength after welding correlated to the decrement in grain size and the formation of $M_{23}C_6$ precipitates [31]. The effect of N on strengthening a CoCrFeMnNi HEA was investigated. The alloys were friction stir processed (FSP), and the yield strength and ultimate tensile strength increased due to N solid solution and grain boundary strengthening [32]. As-cast and rolled CoCrFeMnNi HEAs were welded by FSW [33]. More considerable resistance to plastic deformation during FSW was observed for the as-cast HEA, attributed to the higher density of high-angle grain boundaries and twins in the as-cast condition [33]. The cast and rolled FSW welded CoCrFeMnNi HEA had a higher room temperature strength than the base metal [34]. The cryogenic strength was also improved owing to the primary twin, secondary twin, and tangled dislocation [34]. The comparison between laser welding (LW) and FSW for a CoCrFeMnNi HEA was carried out, and the tensile strength and fracture elongation of FSW and LW welds were comparable to that of annealed base material [35].

Sound joints without welding defects were obtained for a single-phase FCC $CoCrFeNiAl_{0.3}$ HEA [36]. A single-phase FCC $Al_{0.1}CoCrFeNi$ HEA was FSP, and a notably high elongation was achieved for the FSP alloy [37]. A single phase FCC $Co_{16}Fe_{28}Ni_{28}Cr_{28}$ HEA was welded by FSW, and discontinuous dynamic recrystallisation (DDRX) was identified as the restoration mechanism at the SZ, forming a {112}<110> shear texture [38]. A single-phase FCC $Al_{0.3}CoCrCu_{0.3}FeNi$ HEA was FSW welded. It showed a yield strength of 920 MPa with an elongation of 37 % attributed to the partially recrystallised heterogeneous structure formed in the SZ [39].

A metastable $Fe_{40}Mn_{20}Co_{20}Cr_{15}Si_5$ HEA FS welded exhibited good mechanical properties for all the zones, including higher strength and fraction elongation in the SZ [40]. The microstructure and mechanical properties of a FS welded dual-phase $Al_{0.5}CoCrFeNi$ multi-principal element alloy were investigated, and a refined microstructure was formed at the SZ [41]. A heterogeneous bimodal-grained $Al_xCoCrFeNi$ HEA was produced via FSP with the addition of Al powders [42]. Fine Al-rich BCC phase was formed due to the Al additions. As a result, the strength was increased, and fracture elongation was retained as compared with the FSP base alloy [42]. FSP was also applied to refine the microstructure of a dual phase $AlCoCrFeNi_{2.1}$ eutectic high-entropy, increasing the strength from ~1000–1360 MPa and the fracture elongation from ~6.5 to 10 % [43].

Although the feasibility, microstructure and their impact on the mechanical properties of FSW were already investigated for multi-principal alloys, the mechanisms for microstructure and texture formation in FSW of MEAs and HEAs still need to be further investigated. Since the FSW of austenitic stainless steels has been investigated in detail [44–51] and their texture has also been characterised by various thermomechanical processes [52–56], this work compares the microstructure of FSW welds of FCC CoCrNi MEA and CoCrFeMnNi HEA with an FSW weld of a commercial stainless steel AISI 304.

Therefore, this work aims to clarify the mechanisms related to the microstructure modifications concerning the possible deformation and recrystallization phenomena and their interactions in forming the different zones of the produced welds. The microstructure of the cross-sections of the welds is characterised using electron backscattered diffraction (EBSD), and the main microstructural features are obtained and discussed, i.e., low and high angle grain boundaries, local misorientation and orientation spread. The deformation and restoration mechanisms are inferred and correlated to the crystallographic texture formed in the different regions of the weld.

2. Experimental procedures

A commercial hot rolled stainless steel AISI 304, a MEA and a HEA were welded by FSW. The CoCrFeMnNi HEA and CoCrNi MEA were prepared by vacuum induction melting pure elements (purity: 99.9 wt %) and homogenised at 1200 °C for 48 h afterwards. The material preparation is described in more detail in [57,58]. The ingots with a diameter of 40 mm were rotary swaged to a diameter of 16 mm. Afterwards, the ingots were additionally recrystallised at 1020 °C (HEA) and 1060 °C (MEA) for 60 min to get a single-phase fcc alloy with some minor production-related impurities (Cr- and Mn-rich oxides) [59]. The sheets for the FSW were electrical discharge machined from the ingots with the dimension of $16\times82\times1$ mm^3 . The chemical compositions of the alloys were determined by electron microprobe analysis (EMPA) for HEA and MEA, as well as the optical emission spectroscopy (OES) analysis for the stainless steel AISI 304, and are listed in Table 1.

Butt-joints were produced using the thin sheets, which were welded using a 5-axis machining centre DMU 65 (DMG MORI), as shown in Fig. 1a. The movement of the tool was path-controlled. Beneath the sheets, an alumina plate was used as a support base during FSW. Fig. 1 shows the experimental setup. The FSW tool (Fig. 1b) consisted of a sintered W alloy with 1.5 wt % La_2O_3. The tool shoulder (diameter: 8 mm) was concave. The tool pin was 0.9 mm long and conical (diameter: 2.0–2.4 mm), and a new tool was used for every weld. In addition, three surfaces on the pin were machined as seen in Fig. 1b to aid material transport. During the test, the tool was set at 2° against the feed direction. The plunge speed was 10 $mm{\cdot}min^{-1}$, the rotation speed 3000 min^{-1} and the feed speed 100 $mm{\cdot}min^{-1}$. Because of the higher melting point of the CoCrNi MEA compared to the HEA, an increased depth of entry by 0.05 mm of the tool to the specimen was used to reach the

Table 1
Chemical composition (in atomic %) of CoCrFeMnNi HEA and CoCrNi MEA by EMPA and AISI 304 by OES analyses (for AISI 304, only main alloying elements are listed).

	Co	Cr	Fe	Mn	Ni
HEA	19.7	20.7	19.6	20.1	19.9
MEA	33.0	34.3	-	-	32.7
AISI 304	-	20.4	70.2	1.6	7.8

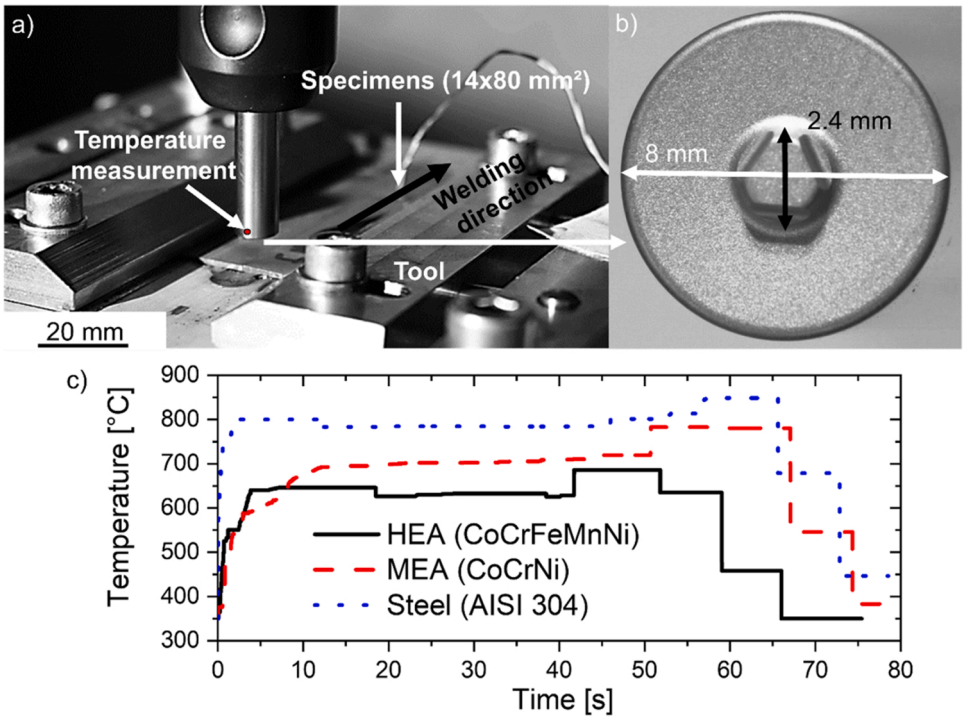

Fig. 1. a) photo of the experimental setup for the friction stir welding carried out in this work [60]; b) bottom view of the tool used; c) measured temperature profiles from the thermocouple inserted in the welding tool as indicated in a).

required temperature. The temperature evolution during the process was measured in the tool as indicated in Fig. 1c. The highest and lowest temperatures were achieved for the welding of the 304 L and HEA, respectively.

Cross-sections of the produced welds were cut and metallographically prepared by grinding up to grit 2000 silicon carbide papers, followed by polishing with silicium-oxide polishing suspension (OP-S). The polished samples were investigated using a Tescan Mira 3 scanning electron microscope (SEM) equipped with an EDAX Octane Plus energy dispersive X-ray spectroscopy (EDX) detector and a Hikari Plus electron backscattered diffraction (EBSD) camera. Backscattered electron (BSE) micrographs were acquired using a voltage of 15 kV, a spot size between 30 and 50 nm and a working distance between 12 and 15 mm. Multiple EBSD maps were acquired for a step size of 1.5 μm and merged so the whole cross-section of the weld was measured. In addition, The EBSD data were treated using OIM Data Analysis v8.6. First, the data was cleaned, standardising the confidence index of a grain considering a minimum grain size of 5 pixels for a transition angle between low (LAGB) to high angle grain boundaries (HAGB) of 15°. Then, the data was cleaned using grain dilation for pixels with a confidence index smaller than 0.1. Afterwards, pixels with a confidence index smaller than 0.1 are considered non-indexed. The merged EBSD measurements were then cropped in smaller areas, which were evaluated individually. The mean values of the microstructural features of these areas were plotted for the cross-section. The coincidence site lattice (CSL) Σ3 (111) were evaluated considering a tolerance of $15/(\Sigma 3)^{0.5}$. The kernel average misorientation (KAM) was calculated using the first neighbour. The geometric necessary dislocation (GND) density was calculated for the $\{111\}<1\bar{1}0>$ slip system using the first neighbour. Grain orientation spread (GOS) was calculated considering a grain as an area surrounded by HAGB without excluding the CSL boundaries. The crystallographic texture was evaluated using the harmonic series expansion up to the 16th series rank for a Gaussian Half-Width of 5° without sample symmetry using the average orientation of each grain. For the individual maps, the maximum texture index of the (001), (011) and (111) pole figures were calculated.

3. Results

The microstructure of the cross-section of the welds was characterised using SEM assisted by EBSD. The different zones are compared regarding their microstructural features and crystallographic texture.

3.1. Austenitic stainless steel AISI 304

A few zones can be identified in an FSW weld, namely stirred zone (SZ), thermomechanical affected zone (TMAZ), and heat-affected zone (HAZ). The SZ corresponds to the dynamically recrystallised zone, where the heavily deformed material forms the nugget in the central part of the weld. Post-dynamic recrystallisation can also occur in the SZ due to the high stored energy due to the high strains and strain rates combined with relatively slow cooling rates [61]. The TMAZ corresponds to the region that underwent plastic deformation during the FSW. However, recrystallisation is limited or does not occur in this zone due to insufficient deformation. The HAZ of transformable steels is associated with the phase transformations that occur and the impact of temperature on the ferrite size and morphology [30]. Here, the MEA and HEA are single-phase alloys and do not suffer allotropic transformations or precipitation. Presence of small δ-ferrite grains in specific regions of the SZ immerged in the FCC austenitic matrix are reported in its FSW welds of AISI 304 [45,51,62,63]. Thus, the HAZ of the investigated welds is interpreted as the region that suffers microstructural changes differentiating it from the base metal without involving plastic deformation. The microstructural changes in the HAZ occur either due to static recrystallisation and/or grain coarsening.

The microstructure of the cross-section of the friction stir weld of AISI 304 steel is shown in Fig. 2, and the following welds zones are observed:

- The FZ is composed of a slightly refined microstructure formed by dynamic and post-dynamic recrystallisation [61], as seen by the high boundary density in Fig. 2d. The high GOS and KAM values in Fig. 2b indicate that post-dynamic recrystallisation is limited in this region.

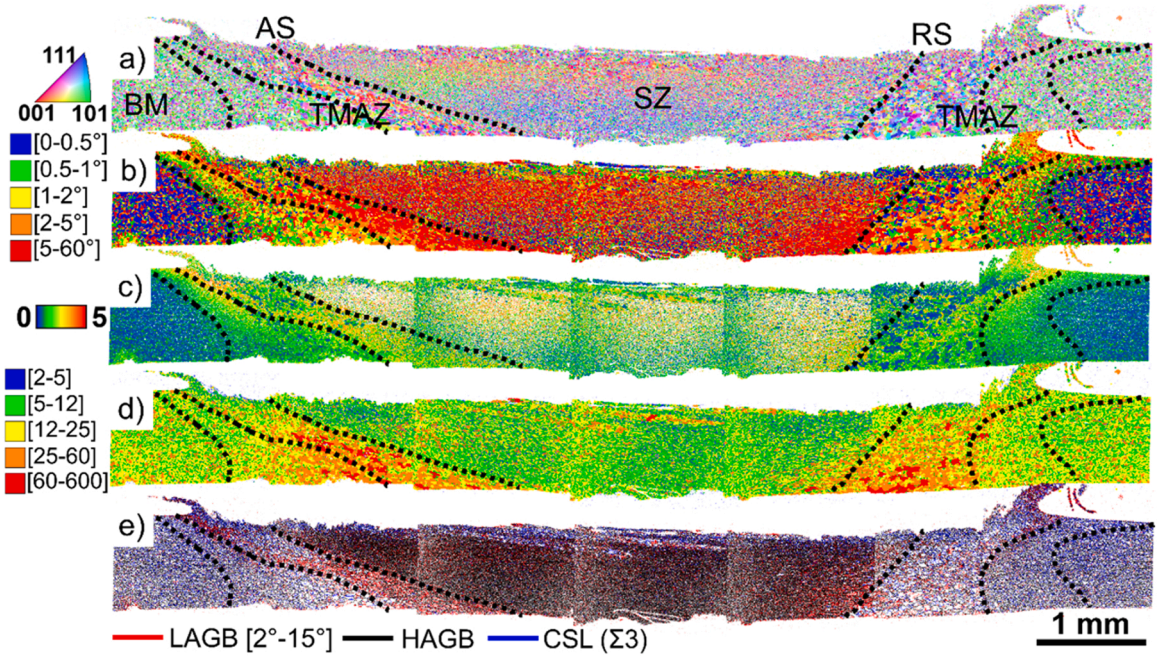

Fig. 2. Electron backscattered diffraction (EBSD) maps of the cross-section of the friction stir welds of the austenitic stainless steel AISI 304: a) inverse pole figure map; b) grain orientation spread (GOS) map; c) kernel average misorientation (KAM) map; d) grain size map; e) boundary map. The dashed lines indicate the possible separation line between the different zones of the weld.

- A first TMAZ near the nugget where: a) a region with grains with high GOS and high density of LAGB are formed in the bottom part of the advancing side (AS); b) a fine microstructure with high values of KAM in the neighbour region of the flash in both advancing side (AS) and retreating sides (RS); III) a zone with large partially recrystallised grains on the RS.

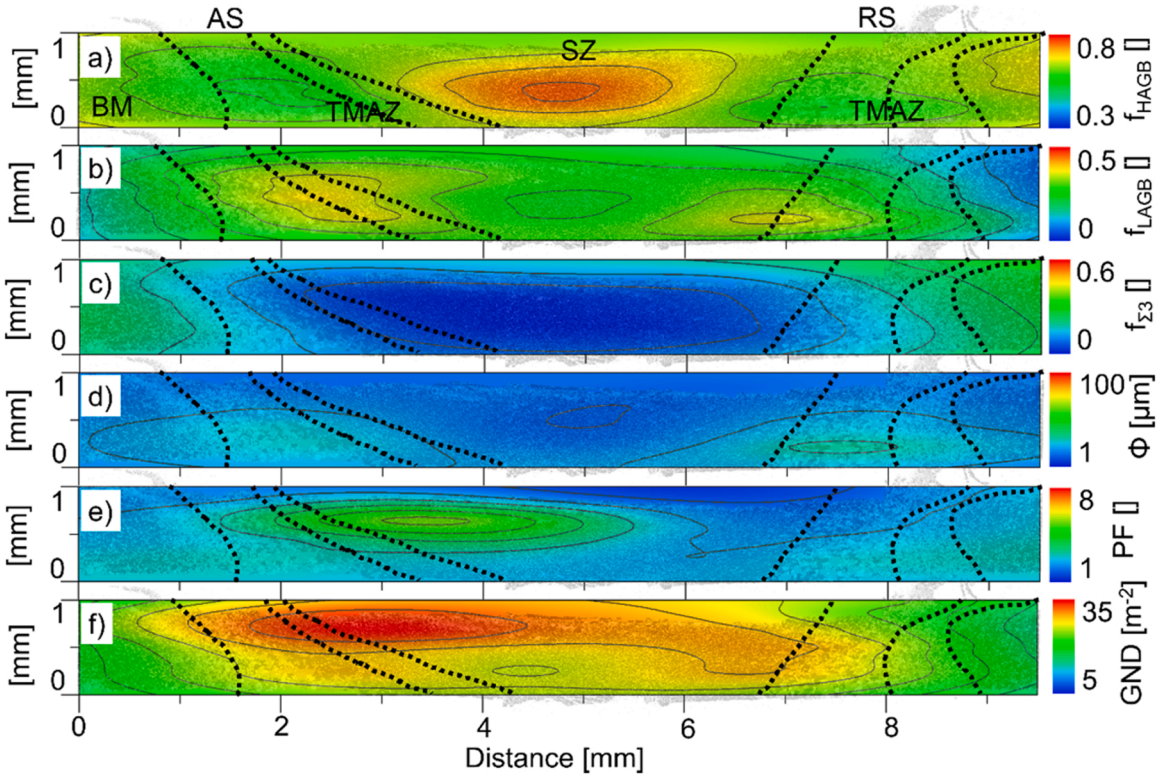

Fig. 3. Contour maps overlayed with the inverse pole figure map for the friction stir weld of the AISI 304 showing the distribution of a) the fraction of high-angle grain boundaries excluding Σ3 boundaries; b) the fraction of low-angle grain boundaries; c) the fraction of Σ3 boundaries; d) the average grain size; e) the maximum index of texture calculated for the (001), (110) and (111) planes; f) geometric necessary dislocation (GND) density. The black dashed lines indicate the possible separation line between the different zones of the weld in Fig. 2.

- A second TMAZ near the base metal (BM) where a gradient from large, deformed grains with high GOS and KAM values to smaller grains is observed towards BM.
- There is no evidence of microstructural changes related to static recrystallization or grain coarsening near the BM in a region without plastic deformation. Thus, no HAZ could be identified. Instead, the plastic deformation promoted by FSW forms two TMAZ that have a transition directly to the BM.

Fig. 3 shows the contour maps calculated by cropping the EBSD measurement of the cross-section of the friction stir weld of AISI 304 shown in Fig. 2 and analysing the separated areas. LAGBs are formed in a high fraction in the TMAZ and the outer regions of the SZ, as shown in Fig. 2d and Fig. 3b. The fraction of Σ3 is notably small in the SZ and the first TMAZ in the AS, as shown in Fig. 3c. The fraction of HAGB is maximum at the central region of the nugget and minimum at the TMAZ, as shown in Fig. 3a. The recrystallisation during deformation and cooling partially restores and refines the microstructure in the SZ. The average grain sizes as small as 2 μm are measured in the SZ, as shown in Fig. 3d. The average grain size is slightly higher in the bottom region of the second TMAZ than in the BM. This part of the weld is subjected to high temperatures for longer times as there is lower heat dissipation on the bottom part of the weld since an alumina plate was used as the base during FSW. The second TMAZ is subjected to low deformation levels since it is far from the pin and the shoulder. The large and partially recrystallised grains formed in this region indicates that plastic deformation and high temperatures lead to DDRX followed by fast grain growth during post dynamic recrystallization.

The crystallographic texture is a microstructure feature directly related to the level of isotropy in the material. The higher the texture index, the more anisotropic the material is expected to be. Fig. 3e shows the contour map for the maximum texture index among the (100), (110), and (111) pole figures. The highest values are measured in the AS of the nugget near the TMAZ, forming a region parallel to the shoulder that only extends to ~100 μm along the thickness. Lower values of the maximum texture index are measured on the RS in the region that was in contact with the shoulder as well as in the upper part of the TMAZ in the RS.

The GND correspond to the dislocations required to accommodate the lattice curvature that arises whenever there is a non-uniform plastic deformation [64]. They do not contribute to plastic strain, but they act as obstacles to the motion of other dislocations, contributing to the work hardening of the material. Thus, high GND density values are expected for deformed materials. Fig. 3f shows the contour map for the GND density distribution in the AISI 304 weld. High values are observed on the top side of the AS of the nugget, and it extends towards the TMAZ. The maximum values are found near the interface with the TMAZ in the AS. The GND density values gradient decreases from the centreline towards the BM on the RS.

Overall, Fig. 3 shows that the FSW produced a heterogeneous microstructure in the AISI 304 weld when comparing the different zones and the AS vs RS. A finer microstructure with a notably low fraction of Σ3 boundaries is formed in the nugget compared to the BM. The nugget's top part shows higher values of GNDs, maximum texture index, and a relatively high fraction of LAGBs. Apart from the low values of the maximum texture index measured on the upper part of the SZ and the high fraction of LAGB measured in the vicinity of the TMAZ, the nugget in the RS shows no particular "peak" for the other microstructural features. It mainly consists of a refined microstructure with a low maximum texture index. The TMAZ near the nugget has a fine microstructure on the AS, while it is coarser on the RS. The TMAZ near the BM has large grains in the bottom region of the AS. The fraction of LAGB is high for all TMAZ, but the texture is weak in the RS and pronounced in the AS. The GND values are higher in the TMAZs in the AS than in the RS.

The complex thermomechanical processes that occur during the FSW strongly modify the microstructure of the AISI 304, as shown in Fig. 2 and Fig. 3. The maximum index of texture is shown in Fig. 3e. Fig. 4a shows the (111) pole figures for the different cropped areas of the weld. The base metal has a strong {123}<634> S-type texture, as also shown in the orientation distribution function maps in Fig. 4e. The shear forces rotate the crystals in the TMAZ, which is seen in the pole figures by a slight rotation of the main poles in the regions of the TMAZ near the BM. The regions of the TMAZ closer to the nugget are subjected to higher temperatures and shear rates. The plastic deformation is also followed by DDRX due to high temperatures and post-dynamic recrystallisation during cooling. Their complex inter-dependency strongly affects the shear-type of texture formed in the TMAZ and SZ [61]. Thus, recrystallisation partially destroy the {123}<634> S-type texture in the TMAZ. The upper region of the TMAZ near the BM in the AS shows multiple components, but no specific fibre or component is identified. In contrast, a distorted initial {123}<634> S-type texture is observed in the bottom region of the TMAZ near the BM in the AS.

The SZ is subjected to intense plastic deformation and a strong rotated <001>//ND θ-fibre is formed in the AS, which is more pronounced in the central part of the nugget, as shown in Fig. 4c. ND represents the direction of the main axis of the normal forces during plastic deformation. The θ-fibre rotation changes progressively from the TMAZ towards the centreline. Incomplete <001>θ-fibre textures are formed in the AS region of the nugget near the shoulder. The texture formed in the bottom part of the AS of the nugget does not visibly show a θ-fibre but rather multiple texture components. The TMAZ near the nugget in the AS shows a strong θ-fibre in the central region, while multiple components are observed in the upper and bottom regions.

There is a pronounced difference in texture formation between the AS and RS. The texture type on the RS of the nugget has an incomplete <001>θ-fibre texture only near the centreline in the central region of the nugget. A rotated and disperse {110}<110> Goss texture is observed in the regions of the nugget near the TMAZ in the RS, as shown in Fig. 4d. Multiple components are identified in the TMAZ near the nugget in the RS instead of a specific fibre or component.

3.2. MEA

The microstructure of the cross-section of the friction stir weld of the MEA is shown in Fig. 5. The following zones can be identified in the weld:

- The SZ forms a larger nugget than the one for the AISI 304 shown in Fig. 2. Overall, a more recrystallised microstructure with lower KAM and GOS values and a low density of LAGB is observed in the SZ of the MEA compared to the AISI 304 (Fig. 2). The intense DDRX and post-dynamic recrystallisation are responsible for the high density of Σ3 boundaries, typical of recrystallized or annealed microstructures. As a result, the microstructure of the nugget is also refined compared to the one in the BM.
- A TMAZ between the SZ and the BM where a gradient from deformed grains with high GOS and KAM values and some LAGBs is formed towards the annealed microstructure of the BM.
- There is no evidence of microstructural changes related to static recrystallisation and/or grain coarsening in the BM in a region without plastic deformation. Since the BM was welded in the annealed state with relatively large grains, there is no stored energy for static recrystallisation, and grain coarsening would require high exposure times to high temperatures, which is not the case. Thus, no heat-affected zone (HAZ) could be identified. Instead, the plastic deformation promoted by FSW forms one TMAZ that have a transition directly to the BM, which is a significant similarity to the stainless steel presented in the previous chapter.

Fig. 6 shows the contour maps of the MEA obtained in the same way as for the AISI 304 (Fig. 3): cropping the EBSD measurement shown in Fig. 5 and analysing the separated areas. The SZ of the MEA is notably

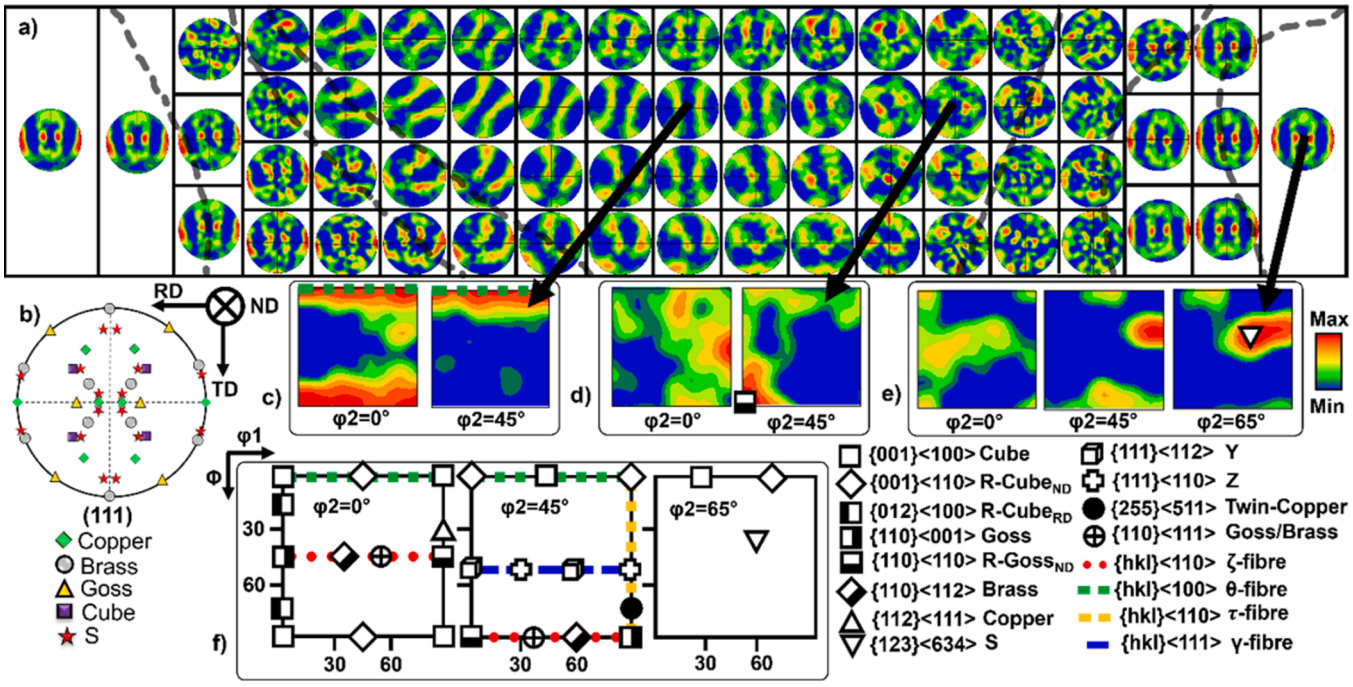

Fig. 4. (111) pole figures of the representative regions of the friction stir weld for the AISI 304. The maximum intensities can be interpreted from Fig. 3e, and the respective zones can be seen in Fig. 2.

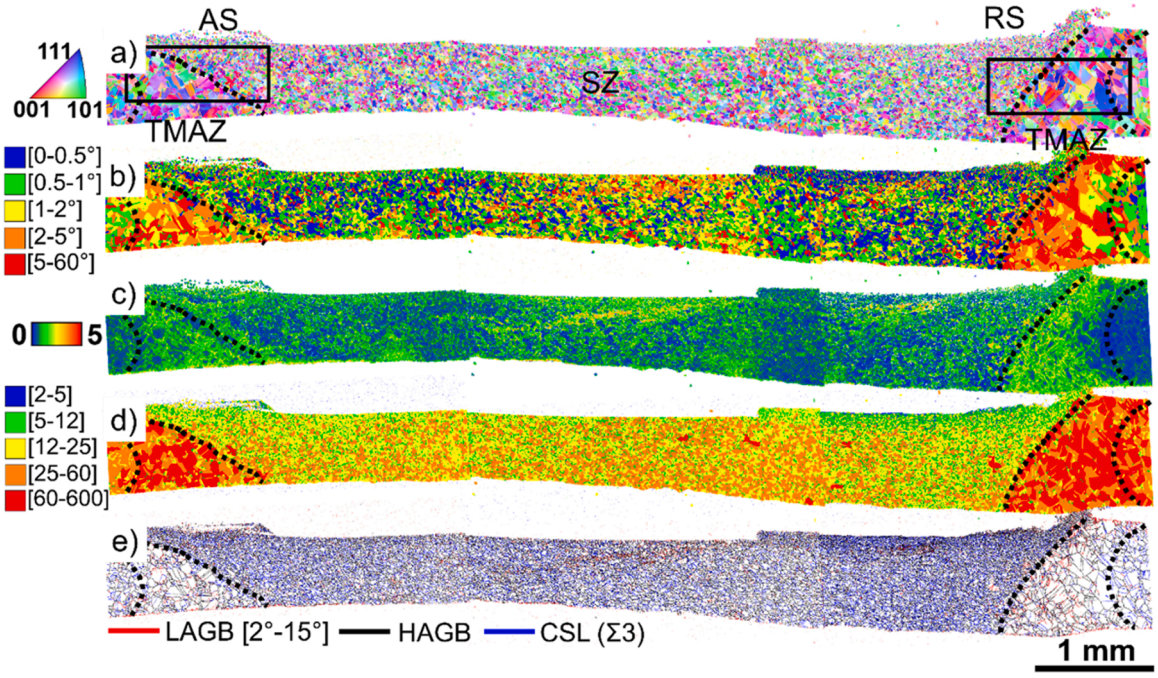

Fig. 5. Electron backscattered diffraction (EBSD) maps of the cross-section of the friction stir welds of the MEA: a) inverse pole figure map; b) grain orientation spread (GOS) map; c) kernel average misorientation (KAM) map; d) grain size map; e) boundary map. The dashed lines indicate the possible separation line between the different zones of the weld. The black rectangles in a) correspond to the areas shown in Fig. 11.

larger than the one in the AISI 304. The gradients and differences between regions in the weld of MEA shown in Fig. 6 are less pronounced than in the AISI 304 shown in Fig. 3.

Regarding the nugget, the regions with the highest fraction of HAGB are located on the upper region of the AS for the MEA weld instead of the bottom region along the centreline in the AISI 304 weld. The smallest grain size of ~2 μm is found in the nugget's RS, as shown in Fig. 6. The fraction of LAGB is small in the nugget of the MEA weld. Also, the fractions of Σ3 boundaries formed in the SZ are only slightly smaller than the ones formed in the BM, opposite to a sharp decrement in Σ3 boundary fraction observed in the SZ of the AISI 304. The maximum texture index is small in the nugget of the MEA, and the minimum values are found in the central regions of the AS and RS of the nugget, like the minimum fraction of LAGB and grain sizes. The upper region of the nugget in the AS and the bottom region of the nugget in the RS show high values of GND density. Overall, the microstructure formed in the SZ

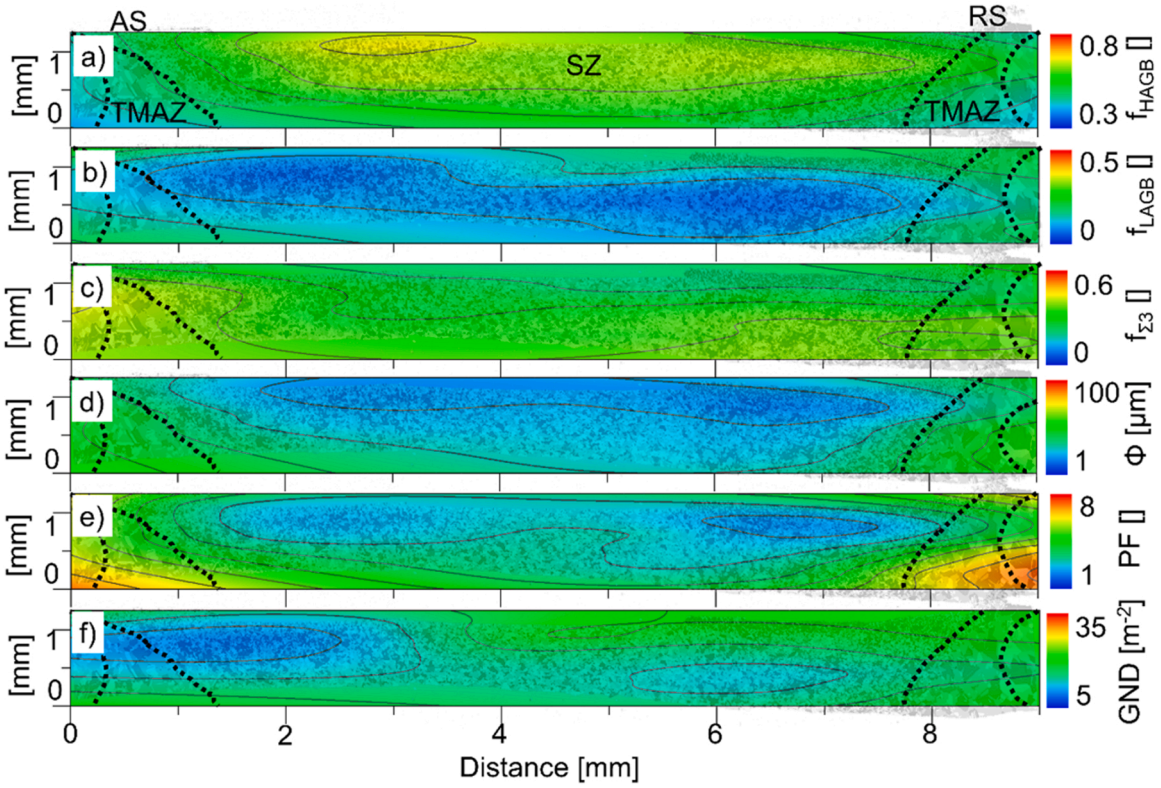

Fig. 6. Contour maps overlayed with the inverse pole figure map for the friction stir weld of the MEA showing the distribution of a) the fraction of high-angle grain boundaries excluding Σ3 boundaries; b) the fraction of low-angle grain boundaries; c) the fraction of Σ3 boundaries; d) the average grain size; e) the maximum index of texture calculated for the (001), (110) and (111) planes; f) geometric necessary dislocation (GND) density. The black dashed lines indicate the possible separation line between the different zones of the weld shown in Fig. 5.

of the MEA weld is slightly coarser but more homogeneous, more isotropic and with lower GOS values, thus with less stored energy after deformation (Fig. 5b) than the SZ formed in the AISI 304 weld.

The TMAZ has a similar grain size to the BM but higher fractions of LAGB due to the plastic deformation. The gradient in plastic deformation is indicated by the gradient in KAM and LAGB, as shown in Fig. 5d and Fig. 6c, respectively.

The crystallographic texture is weaker in all zones of the MEA weld (Fig. 6) than in the AISI 304 weld (Fig. 3). Fig. 7a shows the (111) pole figures measured for different regions of the weld, and only in the central region of the SZ, a more defined rotated {110}<110> Goss-type texture is observed, as shown in Fig. 7b. Multiple components instead of a specific fibre or component are identified in the BM and in other regions of the weld in Fig. 7a.

3.3. HEA

The microstructure of the cross-section of the friction stir weld of the HEA is shown in Fig. 8. The following zones can be identified in the weld:

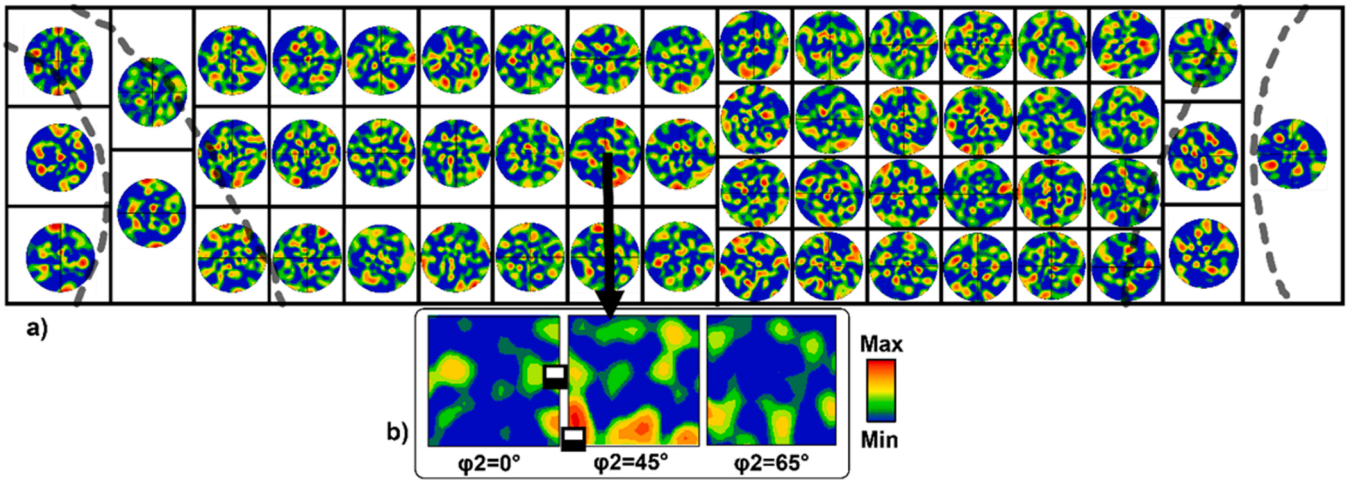

Fig. 7. (111) pole figures of the representative regions of the friction stir weld for the MEA. The maximum intensities can be interpreted from Fig. 6e, and the respective zones can be seen in Fig. 5.

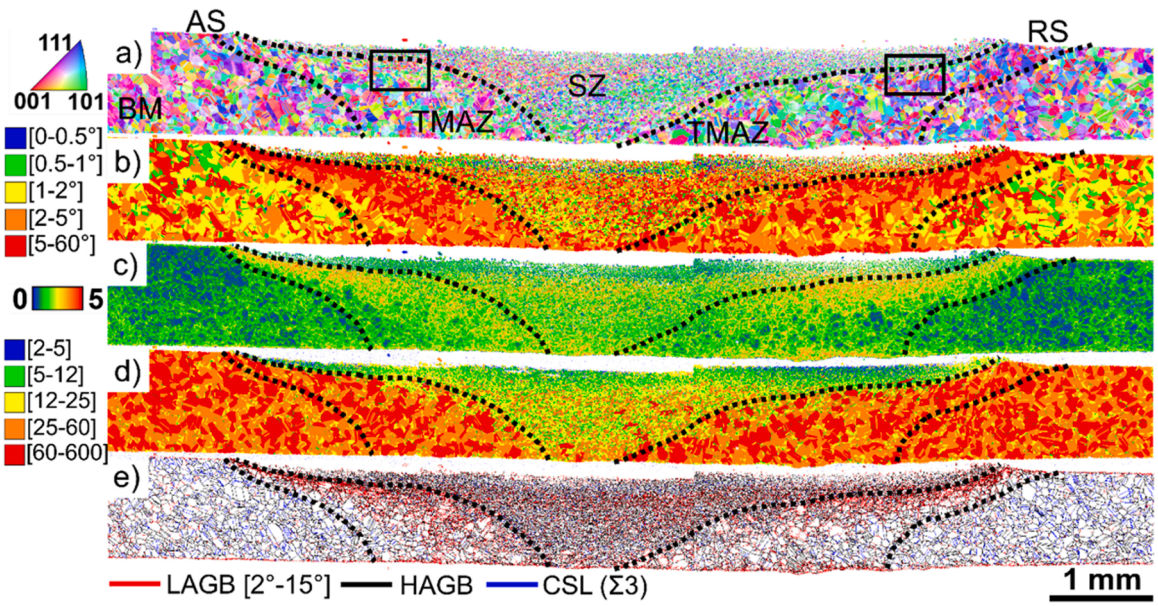

Fig. 8. Electron backscattered diffraction (EBSD) maps of the cross-section of the friction stir welds of the HEA: a) inverse pole figure map; b) grain orientation spread (GOS) map; c) kernel average misorientation (KAM) map; d) boundary map. The dashed lines indicate the possible separation line between the different zones of the weld. The black rectangles in a) correspond to the areas shown in Fig. 12.

- A relatively small SZ is formed compared to the AISI 304 (Fig. 2) or the MEA (Fig. 5). The nugget follows the shape of the tool used for FSW. The microstructure formed in the SZ of the HEA is more comparable to the one at the SZ of the AISI 304 (Fig. 2) than that of the MEA (Fig. 5).
- A TMAZ between the SZ and the BM consisted of a gradient of deformed grains with high density of LAGB and high GOS and KAM values at the SZ towards BM, which is formed by grains with a high fraction of HAGBs and Σ3 boundaries. Medium values of KAM are observed in the BM, suggesting the annealing was insufficient to recrystallize the microstructure fully or that the thin sheet was

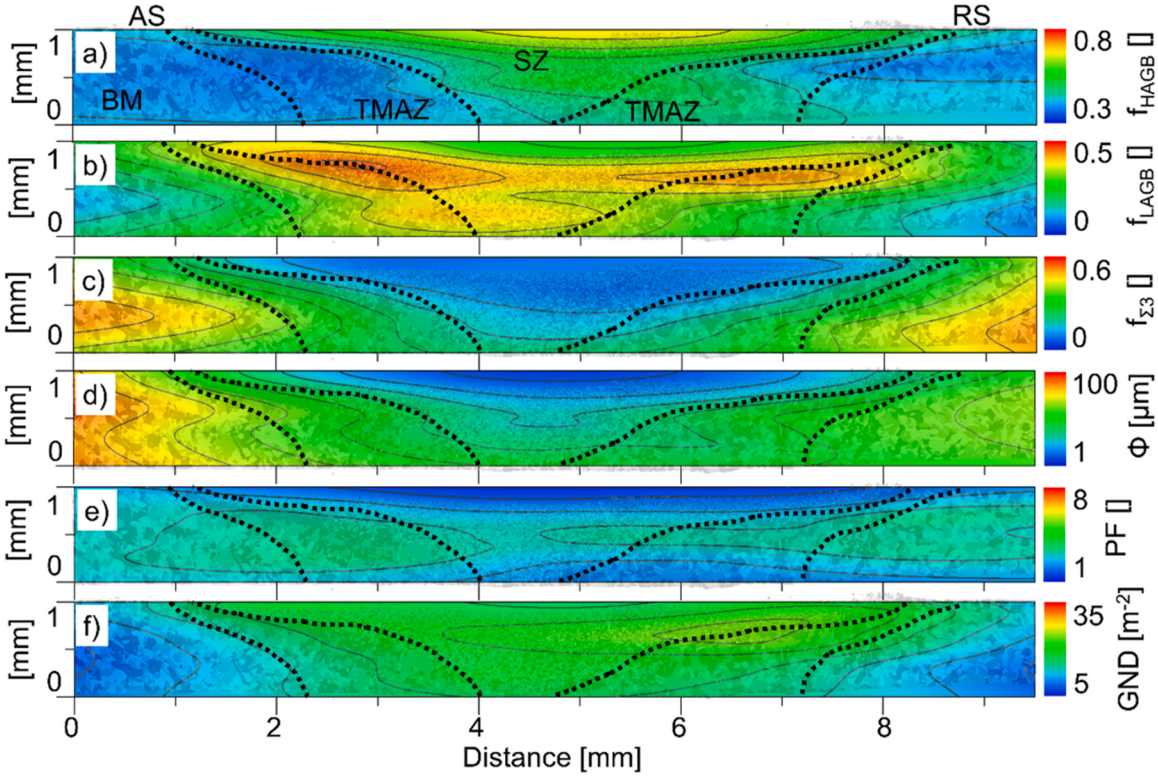

Fig. 9. Contour maps overlayed with the inverse pole figure map for the friction stir weld of the HEA showing the distribution of a) the fraction of high-angle grain boundaries excluding Σ3 boundaries; b) the fraction of low-angle grain boundaries; c) the fraction of Σ3 boundaries; d) the average grain size; e) the maximum index of texture calculated for the (001), (110) and (111) planes; f) geometric necessary dislocation (GND) density. The black dashed lines indicate the possible separation line between the different zones of the weld shown in Fig. 8.

subject to a low level of cold plastic deformation after annealing. Thus, it is not straightforward to define the interface between the TMAZ and the BM.

- Although the BM has medium values of KAM, as shown in Fig. 8c, there is no evidence of microstructural changes related to static recrystallization and/or grain coarsening. Thus, no heat-affected zone (HAZ) could be identified. Instead, the plastic deformation promoted by FSW forms one TMAZ that have a transition directly to the BM, similar to the weld for the AISI 304 (Fig. 2) and the MEA (Fig. 5).

Fig. 9 shows the contour maps of the HEA obtained in the same way as for the AISI 304 (Fig. 3) and the MEA (Fig. 6). Different zones can be distinguished in the weld, and the differences in values for the microstructural features between the different zone is higher than in the MEA weld (Fig. 6) but similar to the ones in the AISI 304 (Fig. 3). However, the shape and size of the SZ are smaller for the HEA than for the AISI 304 or MEA.

Concerning the HEA weld, Fig. 9 shows that the TMAZ zone of the weld has comparable sizes and shapes in both the AS and RS and, to a certain extent, similar microstructures. They are formed by a microstructure that ranges from refined grains with a low fraction of Σ3 boundaries and a high fraction of LAGBs in the regions near the SZ towards the typical microstructure of the BM, formed by larger grains. The texture index is slightly higher in the TMAZ on the AS than in the TMAZ on the RS and the ones measured in the BM. A higher density of GND is formed on the upper region of the RS crossing the TMAZ and the SZ. Two regions with high fractions of LAGB cross the upper regions of the TMAZ towards the SZ in the AS and RS. Refined grains as small as 2 μm are formed in the SZ. The smallest grain size values are observed in the SZ's upper region. The bottom region of the SZ is small, and grain refinement is less pronounced. The decrement in the fraction of Σ3 boundaries within the SZ is notable. Intermediate values of Σ3 boundary fraction between the SZ and the BM are measured in the TMAZ. The fraction of HAGB, though, shows a gradient from the bottom part of the SZ toward the upper region. The central upper region shows the highest values of HAGB fraction. This region also shows a notably lower value of maximum texture index than other regions.

The values of the maximum texture index measured in the HEA weld shown in Fig. 9e are higher than the ones measured for the MEA weld shown in Fig. 6e. However, the (111) pole figures shown in Fig. 10 reveal that it is difficult to specify a fibre or a single texture component in the nugget or the TMAZ for the HEA weld. The texture is slightly more established in the SZ of the HEA than in the SZ of the MEA weld (Fig. 7), where a more defined rotated {110}<110> Goss-type texture is visible, as shown in Fig. 7b. Although the relatively large grain size in the TMAZ could limit the statistical relevance of the data for identifying the texture components in both MEA and HEA welds, that is not the case in SZ, where the grain size is notably smaller.

4. Discussion

The following characteristics control the microstructure formed by FSW [22,65]:

I. The tool geometry and the welding parameters
II. The hot deformation behaviour of the welded material
III. The thermophysical properties of the tool and the welded material are related to temperature dependent material properties.

The boundary conditions given by the complex interactions of I) and III) and the material flow behaviour given by II) determine the temperature and shear rate evolutions during FSW. Those parameters evolve for each region differently. The tool's rotation imposes the material's shear, which flows according to I) and II), forming the SZ. The distribution of stresses and material flow are complex during FSW. It consists of a thermomechanical process where high strain rates are typically achieved in the SZ [54,66], and the material is deformed to effective strains larger than five [54,66]. The achieved temperatures are 80–90 % of the macroscopic melting point, especially near the shoulder and the pin interfaces [54,66]. Microscopically, for materials with micro-chemical segregation, it is possible that small zones with a lower melting point than the macroscopic one locally melt [54,66]. The melting points of the investigated materials in this work are relatively high, and the cooling rate after welding is slow enough to promote post-dynamic recrystallisation, which also has an impact on the microstructure and texture formation [61].

The normal forces applied by the shoulder, the shear forces due to the material stir, and the high temperatures also produce the TMAZ. Here, the total deformation is smaller than in the nugget but sufficient to modify the microstructure substantially. The HAZ in steels that undergoes phase transformation is typically subdivided into several zones associated with the phase transformations that occur and the impact of temperature on the ferrite size and morphology [67]. Here, apart from the AISI 304, where the δ-phase can be present, the MEA and HEA are single phases and do not suffer allotropic transformations or precipitation. Thus, the HAZ of the investigated welds needs to be interpreted as the region where no deformation occurs. However, the high temperatures modify the microstructure, differentiating it from the base metal. Since the initial microstructure was either totally or partially

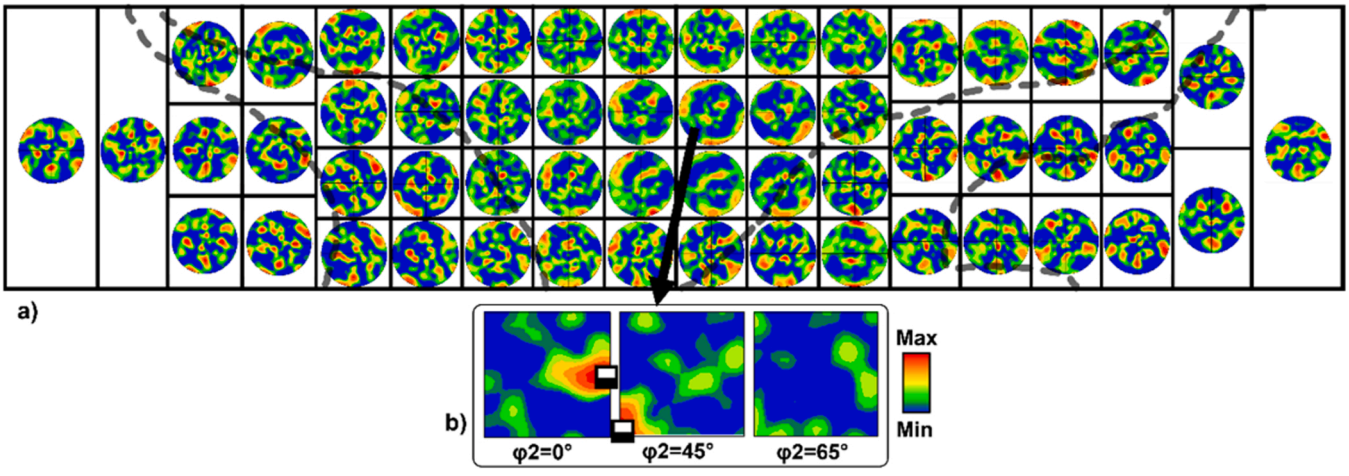

Fig. 10. (111) pole figures of the representative regions of the friction stir weld for the HEA. The maximum intensities can be interpreted from Fig. 9e, and the respective zones can be seen in Fig. 8.

recrystallised, there is little stored energy for static recrystallisation when the material is exposed to high temperatures during FSW. Also, the time and temperatures are insufficient to provoke significant grain coarsening. Thus, as shown in Fig. 2, Fig. 5, and Fig. 8, a HAZ is not evident for the investigated welds.

The tool geometry and the welding parameters were kept constant for the investigated FSW joints. The differences in the microstructure between the welds are, thus, related to the role of the different deformation and restoration mechanisms and their interdependencies with the shear rates and temperatures achieved during FSW. Fig. 11 and Fig. 12 show the EBSD maps for the AS and RS of the upper region of the weld for the MEA and HEA welds, respectively.

The high strain rates and strains achieved at the SZ promote rapid dislocation increment, i.e., work hardening. The shear forces also rotate the grain structure, producing misorientation spread within the grains. Dislocations tend to accumulate along grain boundaries, which are also a source of dislocations since the crystals in neighbouring grains typically rotate differently [68–70]. The KAM maps in Fig. 12(c,d) show high values along the grain boundaries and forming bands. The last is pronounced in the TMAZ of the HEA weld. These arrangements of dislocations and misorientation spread within the grain form a complex substructure with high associated stored energy. When mobile dislocations glide and encounter other gliding dislocations, the following can happen:

- pile up of dislocations, and subsequently be reorganised via dynamic recovery (DRV), forming cells within the microstructure. Intensive pile-ups can form LAGBs, as indicated by the red boundaries in Fig. 11(a,b) and Fig. 12(a,b), mainly at the TMAZ.
- annihilation via DRV.

DRV is intense for high-stacking fault energy materials, and LAGB forms well-established subgrains [71,72]. For those materials, the LAGB evolve to HAGB via continuous dynamic recrystallisation (CDRX), refining the microstructure. The investigated alloys in this work are low-stacking fault energy materials [73–75]. In this case, DRV has a limited role in annihilating or reorganising the dislocations, and a substructure that evolves via a progressive increase of boundary misorientation via CDRX does not occur [71]. For low-stacking fault energy materials, dislocations are pile-ups, and dynamic recrystallisation occurs via nucleation and growth [71,76]. It does not exclude the possibility of forming LAGB since DRV and lattice rotation always occur during plastic deformation [77]. However, the presence of nucleation shows that the role of DRV is limited, and the movement of HAGB and restoration of the microstructure occurs via DDRX. The DDRX extent is higher with increase in stored energy, temperature, and time. In addition, Σ3 boundaries are typically formed during DDRX [71]. For large deformations, a recrystallised grain will be further deformed, and once the stored energy reaches a critical value, nucleation and growth via DDRX occurs again. The cycle repeats multiple times until deformation is finished, leaving a microstructure formed by grains that have been recrystallised and further deformed and freshly recrystallised grains [71].

Once the tool moves away, and the material is still at high temperatures, post-dynamic recrystallisation can occur [61]. It consists of fast nucleation and growth due to the stored energy in the recrystallised and deformed grains [78]. In this case, a fully recrystallised microstructure is formed.

The blue grains in Fig. 11(e,f) and Fig. 12(e,f) correspond to the ones with low misorientation spread or low density of LAGB and can be regarded as recrystallised grains. The low GOS values of the freshly recrystallised grains in the SZ contrast with the high GOS values of the deformed grains in the TMAZ. The high fraction of grains with high GOS values indicates that post-dynamic recrystallisation was sluggish in the SZ for the investigated welds. Some blue grains are seen in the TMAZ. They nucleated likely via DDRX, but the lower temperatures and lower stored energy at the TMAZ hindered the growth of those nuclei. Thus, the SZ can be defined as the region where DDRX occurs intensively, and the microstructure is restored during FSW. A precise location of the interface between the SZ and the TMAZ is impractical, especially for the HEA weld, since there is no sharp boundary between a region with DDRX and a region with low or no recrystallisation. The dashed lines in Fig. 11 and Fig. 12 indicate the possible interface within the range where recrystallised grains are formed or absent.

The shape and size of the nugget are related to the accommodation of plastic deformation by the material, also associated with the temperature distribution, and both are dependent on the deformation imposed by the tool geometry and welding parameters [22,65]. Disregarding the influence of the tool geometry and plate thickness and considering materials with the same melting point, the material with the lowest shear stresses at high temperatures requires lower torque to be

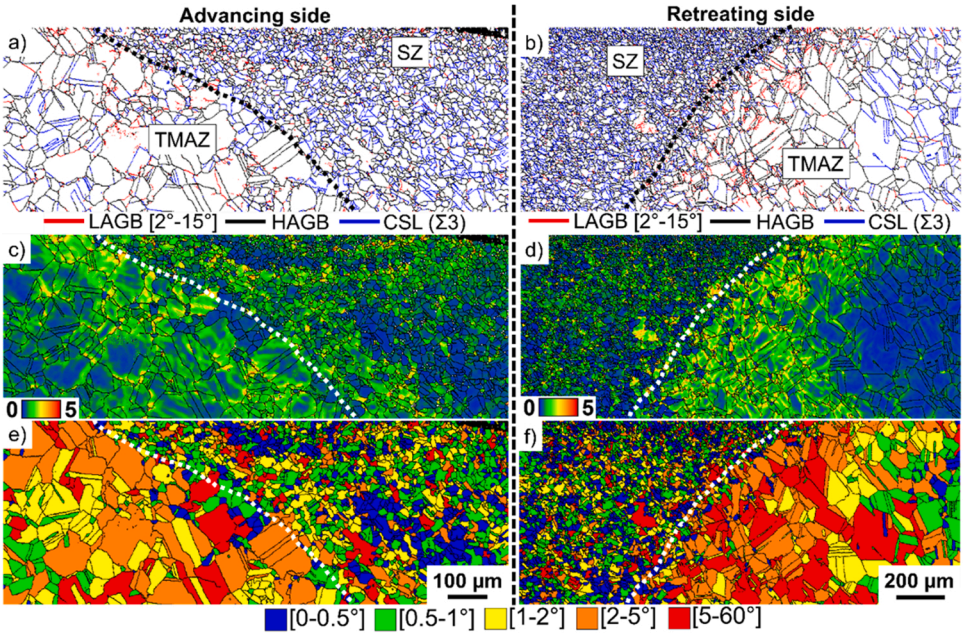

Fig. 11. Electron backscattered diffraction (EBSD) results of the cross-section in the region comprised by the thermomechanical affected (TMAZ) and stir zones (SZ) of the friction stir welds of the MEA shown in Fig. 5 for the (a,c,e) advancing side; (b,d,f) retreating side; showing the: a,b) boundary maps; c,d) kernel average misorientation (KAM) maps; e,f) grain orientation spread (GOS) maps. The dashed lines indicate the possible separation line between the thermomechanical affected zone (TMAZ) and the stir zone (SZ).

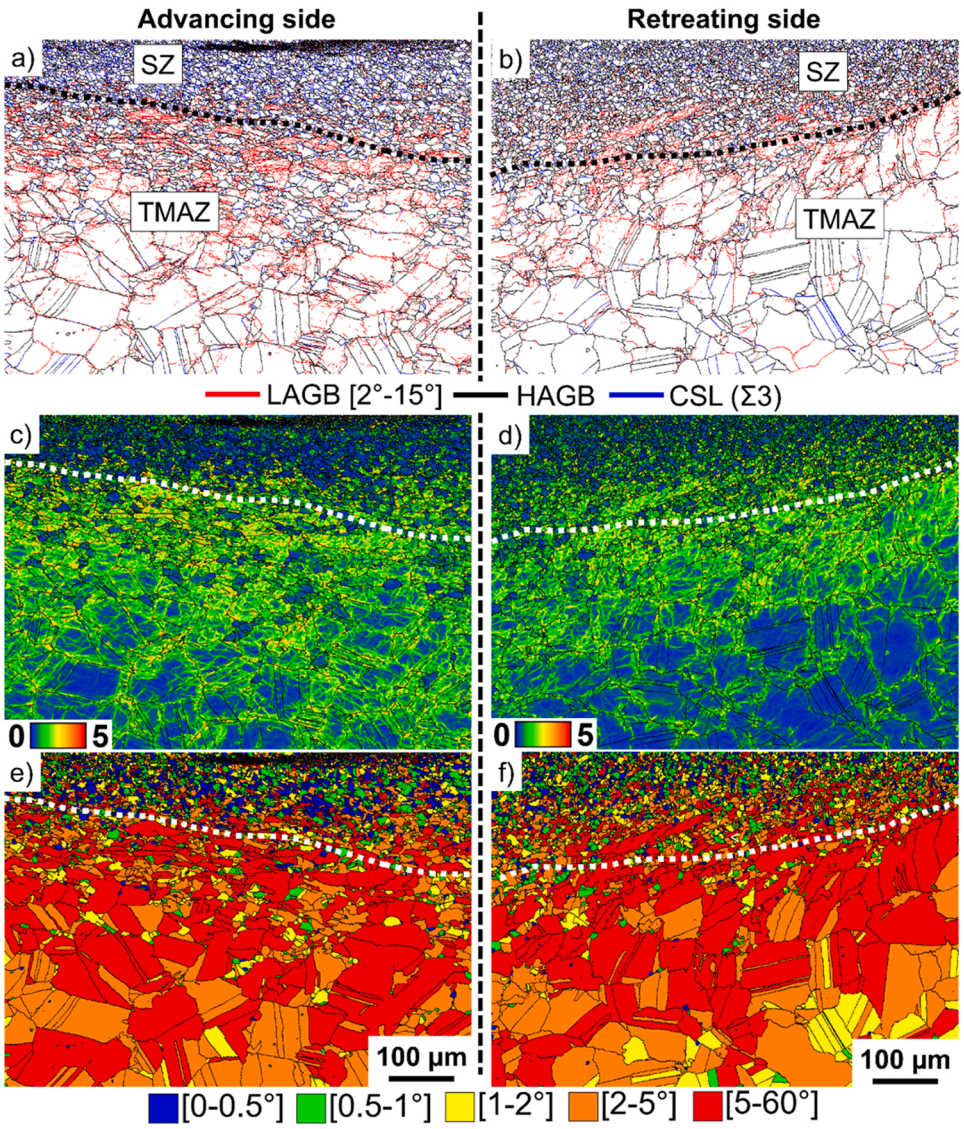

Fig. 12. Electron backscattered diffraction (EBSD) results of the cross-section in the region comprised by the thermomechanical affected (TMAZ) and stir zones (SZ) of the friction stir welds of the HEA shown in Fig. 8 for the (a,c,e) advancing side; (b,d,f) retreating side; showing the: a,b) boundary maps; c,d) kernel average misorientation (KAM) maps; e,f) grain orientation spread (GOS) maps. The dashed lines indicate the possible separation line between the thermomechanical affected zone (TMAZ) and the stir zone (SZ).

deformed. However, the material must be heated via friction with the tool surface. If high temperatures are achieved, the tool does not require high normal forces, and the forging zone ahead of the advancing part of the pin offers less resistance to the tool movement. Another factor is the dependency of the flow stress on strain rate and temperature. If the dependency on temperature is high, the hotter regions around the shoulder and the pin deform intensely, while the colder areas offer high resistance to deformation. Conversely, the temperature distribution will govern the material flow if the material has a low strain rate dependency.

The melting point of the MEA is expected to be ~1420 °C [79,80], similar to the AISI 304, while the HEA has a melting point of ~1280 °C [81]. Fig. 1c shows that the highest temperatures at the shoulder were achieved for the 304 followed by the MEA. The MEA had a larger nugget than the AISI 304, indicating an overall higher heat input for the AISI 304 than for the MEA. The higher energy input was insufficient to promote the same extent of DDRX for the AISI 304 than for the MEA, indicating DDRX is probably faster for the MEA than the AISI 304 for the temperatures and shear rates achieved in the FSW trials in this work. Fig. 1c shows that the smallest temperatures were achieved in the HEA weld, also related to the slower melting point of this material in comparison to the investigated MEA and the AISI 304, which also has the smallest SZ among the investigated welds. It indicates that the lower temperatures achieved in the HEA modified a smaller portion of the material, and DDRX and post dynamic recrystallisation were also limited, as indicated by the high KAM and GOS values in Fig. 8(c and d, respectively).

The low fraction of Σ3 is not related to the absence of twins or DDRX. Instead, it is mainly related to the following:

- The small grain size formed in the SZ: Not every grain is formed with a Σ3, especially for the HEA. Some nuclei are formed without a clear association with a Σ3 boundary.
- Once formed, further plastic deformation bends the crystal structure, decreasing the angle of the formed Σ3 boundaries, which are no longer identified as so in the EBSD measurements.
- Several LAGBs are formed, especially for the HEA, forming a substructure within the deformed grains. Since there is no distinguishment between deformed and recrystallised grains, the overall Σ3 boundary density is small in the SZ. However, its surface density is higher than in the coarser BM for the MEA and HEA welds.

The reasons for different crystallographic textures and intensities between the investigated materials and between the formed regions of the FSW welds are related to the mechanisms of deformation and restoration of the microstructure. The rotated < 001 > fibres observed

for the AISI 304 correspond to the θ-fibre in FCC metals, typically associated with plastic deformation [82]. The rotation of those fibres in the SZ is related to the tensor of plastic deformation during FSW. In the AS, the shear rate is maximum as the rotating and advancing speed sum up. The presence of θ-fibre in the nugget of the AISI 304 weld and its absence in the medium and HEA welds indicate that:

- The role of DDRX and post-dynamic recrystallisation is insufficient to modify the deformation texture formed due to the high shear rates in the AS or the region around the centreline for the AISI 304: which is also evidenced by the weaker texture and formed by multiple components in the RS as well as in the TMAZ. In the RS, the shear rates are lower since the advancing and rotating speeds are in opposite directions. In the TMAZ, recrystallisation occurs due to plastic deformation, modifying the texture of the BM.
- The DDRX and post-dynamic recrystallisation occur faster in the MEA and HEAs than in the AISI 304, modifying and weakening the deformation texture. Thus, the typical deformation texture components and fibres expected for AISI 304 and related FCC alloys are barely formed in the MEA and HEAs. It is also evidenced by the higher fraction of Σ3 boundaries formed in the SZ of the MEA and HEA welds than in the SZ of the AISI 304.
- Transformation to and from δ-ferrite and, consequently, formation of small δ-ferrite grains are reported in other works [45,51,62,63], and the possibility of rapid formation of σ-phase [50] are extra-factors that can occur in FSW welded AISI 304. They can hinder the movement of grain boundaries, consequently diminishing the DDRX kinetics and Σ3 boundary formation.

Table 2 summarises the main microstructural features measured in the different regions of the investigated welds. Complementarily, Table 3 summarises the main deformation conditions and lists the involved phenomena for the microstructural changes in the different weld regions.

Table 2
Summary of the microstructural features for the different regions of the investigated welds of the AISI 304, MEA and HEA.

Material	Regions		Average grain size [μm]	Σ3 boundary fraction [%]	LAGB fraction [%]	Texture
AISI 304	BM		~15	~25	~8	well-established {123}< 634> S-type
	TMAZ	AS-near BM	15–30	15–25	8–30	Multiple components
		AS-near SZ	10–50	10–20	12–45	Multiple components
		RS-near BM	15–30	10–20	8–30	distorted {123}< 634> S-type
		RS-near SZ	10–40	1–20	20–55	Multiple components
	SZ	AS	10–20	1–15	20–40	Rotated <001>θ-fibre or multiple components
		RS	10–20	1–15	20–40	Rotated {110}< 110> Goss or multiple components
MEA	BM		~60	~40	~8	Multiple components
	TMAZ		50–80	15–40	10–30	Multiple components
	SZ		10–30	15–40	5–20	{110}< 110> Goss or multiple components
HEA	BM		~60	~40	~10	Multiple components
	TMAZ		40–60	15–40	10–60	Multiple components
	SZ		10–30	5–20	30–50	{110}< 110> Goss or multiple components

5. Summary and conclusions

Butt joints were produced using friction stir welds for a commercial stainless steel AISI 304 and two multi-principal alloys: a CoCrFeMnNi HEA and a CoCrNi MEA. The welds were produced with the same plunging, rotation and advancing speeds and were characterised using SEM assisted by EBSD. The results allow the following conclusions:

- Grain refinement occurs in the SZ of all welded materials. The size of the SZ formed in the MEA and HEA welds is the largest and the smallest, respectively.
- The HAZ of the investigated welds needs to be interpreted as the region where no deformation occurs. Since the initial microstructure was either totally or partially recrystallised, there is little stored energy for static recrystallisation when the material is exposed to high temperatures during FSW. Also, the time and temperatures are insufficient to provoke significant grain coarsening. Thus, a HAZ is not evident for the investigated welds.
- Although it is not possible to distinguish DDRX from post-dynamic recrystallisation, DDRX seems to be the predominant restoration mechanism during FSW of the three investigated alloys as high KAM and GOS values are measured in the grains formed in the SZ.
- DDRX is more pronounced and strongly modifies the deformation texture for the MEA and HEA welds compared to the AISI 304 welds.
- A sharp decrement in the Σ3 boundary fraction occurs in the SZ of the AISI 304 and HEA welds due to the high fraction of LAGB. Comparable values of Σ3 fraction between the SZ and the BM are found for the MEA weld.
- For the AISI 304 welds, from a well-established {123}< 634 > S-type texture of the BM, a peak in the maximum index of crystallographic texture is observed on the AS of the SZ in the AISI 304 weld, where a strong < 001 > θ-fibre texture is formed.
- A rotated and distorted {110}<110> Goss texture is observed in the regions of the SZ near the TMAZ on the retreating side in the AISI 304 weld and in the central region of the SZ of the MEA and HEA welds.
- Apart from the mentioned regions with a more-defined texture type, multiple components are identified in the other weld regions instead of a specific fibre or component, especially for the MEA and HEA welds.

CRediT authorship contribution statement

Conceptualization: Ricardo Henrique Buzolin, Tim Richter, Florian Pixner, Michael Rhode, Dirk Schroepfer, Norbert Enzinger; **Methodology:** Ricardo Henrique Buzolin, Tim Richter, Florian Pixner; **Formal analysis:** Ricardo Henrique Buzolin; **Investigation:** Ricardo Henrique Buzolin, Tim Richter, Florian Pixner; **Resources:** Michael Rhode, Dirk Schroepfer, Norbert Enzinger; **Writing - Original Draft:** Ricardo Henrique Buzolin, Tim Richter, Florian Pixner; **Writing - Review & Editing:** Ricardo Henrique Buzolin, Tim Richter, Florian Pixner, Michael Rhode, Dirk Schroepfer, Norbert Enzinger; **Visualization:** Ricardo Henrique Buzolin.

Table 3
Summary of the predominant deformation conditions and involved phenomena for the different regions of the investigated welds of the AISI 304, MEA and HEA.

Regions	Deformation	Temperature	Phenomena
BM	None	Regions near the TMAZ might be heated but insufficient for visible microstructural changes	None
TMAZ	Gradient from none at BM to small deformations towards the SZ. In general, sufficiently high for forming LAGB, causing misorientation spread and eventually DDRX	Sufficiently high for DDRX and eventually post-dynamic recrystallisation	Dislocation increase and misorientation spread formation, i.e. work hardening. In regions subjected to higher plastic deformations and higher temperatures, DDRX and post-dynamic recrystallisation occur.
SZ	Intense plastic deformation	High but below the melting point	The high temperatures, strain rates, and effective strains reached in this region promote DDRX followed by post-dynamic recrystallisation.

Declaration of Competing Interest

The authors declare that they have no known competing financial interests or personal relationships that could have appeared to influence the work reported in this paper.

Acknowledgements

We would like to thank apl.-Prof. G. Laplanche from the Technical University of Bochum, Germany, for providing the materials and Dr.-Ing. M. Schneider from the MTU Aero Engines GmbH, Germany. Ricardo Henrique Buzolin fosters the Christian Doppler Laboratory for Design of High-Performance Alloys by Thermomechanical Processing with the support of the Christian Doppler Society. Open access funding by the Graz University of Technology is also acknowledged.

References

[1] D.B. Miracle, O.N. Senkov, A critical review of high entropy alloys and related concepts, Acta Mater. 122 (2017) 448–511, https://doi.org/10.1016/j.actamat.2016.08.081.
[2] E.P. George, D. Raabe, R.O. Ritchie, High-entropy alloys, Nat. Rev. Mater. 4 (2019) 515–534, https://doi.org/10.1038/s41578-019-0121-4.
[3] M.-H. Tsai, J.-W. Yeh, High-entropy alloys: a critical review, Mater. Res. Lett. 2 (2014) 107–123, https://doi.org/10.1080/21663831.2014.912690.
[4] Y.F. Ye, Q. Wang, J. Lu, C.T. Liu, Y. Yang, High-entropy alloy: challenges and prospects, Mater. Today 19 (2016) 349–362, https://doi.org/10.1016/j.mattod.2015.11.026.
[5] S. Huang, W. Li, X. Li, S. Schönecker, L. Bergqvist, E. Holmström, L.K. Varga, L. Vitos, Mechanism of magnetic transition in FeCrCoNi-based high entropy alloys, Mater. Des. 103 (2016) 71–74, https://doi.org/10.1016/j.matdes.2016.04.053.
[6] F.D.C. Garcia Filho, R.O. Ritchie, M.A. Meyers, S.N. Monteiro, Cantor-derived medium-entropy alloys: bridging the gap between traditional metallic and high-entropy alloys, J. Mater. Res. Technol. 17 (2022) 1868–1895, https://doi.org/10.1016/j.jmrt.2022.01.118.
[7] E.P. George, W.A. Curtin, C.C. Tasan, High entropy alloys: a focused review of mechanical properties and deformation mechanisms, Acta Mater. 188 (2020) 435–474, https://doi.org/10.1016/j.actamat.2019.12.015.
[8] B. Gludovatz, A. Hohenwarter, D. Catoor, E.H. Chang, E.P. George, R.O. Ritchie, A fracture-resistant high-entropy alloy for cryogenic applications, Science (80–.) 345 (2014) 1153–1158, https://doi.org/10.1126/science.1254581.
[9] N. Kumar, Q. Ying, X. Nie, R.S. Mishra, Z. Tang, P.K. Liaw, R.E. Brennan, K. J. Doherty, K.C. Cho, High strain-rate compressive deformation behavior of the Al0.1CrFeCoNi high entropy alloy, Mater. Des. 86 (2015) 598–602, https://doi.org/10.1016/j.matdes.2015.07.161.
[10] P. Shi, W. Ren, T. Zheng, Z. Ren, X. Hou, J. Peng, P. Hu, Y. Gao, Y. Zhong, P. K. Liaw, Enhanced strength–ductility synergy in ultrafine-grained eutectic high-entropy alloys by inheriting microstructural lamellae, Nat. Commun. 10 (2019) 489, https://doi.org/10.1038/s41467-019-08460-2.
[11] N. Kumar Katiyar, K. Biswas, J.-W. Yeh, S. Sharma, C. Sekhar Tiwary, A perspective on the catalysis using the high entropy alloys, Nano Energy 88 (2021), 106261, https://doi.org/10.1016/j.nanoen.2021.106261.
[12] K. Li, W. Chen, Recent progress in high-entropy alloys for catalysts: synthesis, applications, and prospects, Mater. Today Energy 20 (2021), 100638, https://doi.org/10.1016/j.mtener.2021.100638.
[13] M.S. Lucas, L. Mauger, J.A. Muñoz, Y. Xiao, A.O. Sheets, S.L. Semiatin, J. Horwath, Z. Turgut, Magnetic and vibrational properties of high-entropy alloys, J. Appl. Phys. 109 (2011) 07E307, https://doi.org/10.1063/1.3538936.
[14] V. Chaudhary, R. Chaudhary, R. Banerjee, R.V. Ramanujan, Accelerated and conventional development of magnetic high entropy alloys, Mater. Today 49 (2021) 231–252, https://doi.org/10.1016/j.mattod.2021.03.018.
[15] P. Kumari, A.K. Gupta, R.K. Mishra, M.S. Ahmad, R.R. Shahi, A comprehensive review: recent progress on magnetic high entropy alloys and oxides, J. Magn. Magn. Mater. 554 (2022), 169142, https://doi.org/10.1016/j.jmmm.2022.169142.
[16] H. Cheng, Z. Pan, Y. Fu, X. Wang, Y. Wei, H. Luo, X. Li, Review—corrosion-resistant high-entropy alloy coatings: a review, J. Electrochem. Soc. 168 (2021), 111502, https://doi.org/10.1149/1945-7111/ac34d0.
[17] X. Zhang, N. Zhang, B. Xing, S. Yin, An assessment of the high-temperature oxidation resistance of selected thermal sprayed high entropy alloy coatings, J. Therm. Spray. Technol. 31 (2022) 1386–1403, https://doi.org/10.1007/s11666-022-01352-w.
[18] R.K. Nutor, Q. Cao, X. Wang, S. Ding, D. Zhang, J.-Z. Jiang, Accelerated emergence of CoNi-based medium-entropy alloys with emphasis on their mechanical properties, Curr. Opin. Solid State Mater. Sci. 26 (2022), 101032, https://doi.org/10.1016/j.cossms.2022.101032.
[19] Z. Zhang, H. Sheng, Z. Wang, B. Gludovatz, Z. Zhang, E.P. George, Q. Yu, S.X. Mao, R.O. Ritchie, Dislocation mechanisms and 3D twin architectures generate exceptional strength-ductility-toughness combination in CrCoNi medium-entropy alloy, Nat. Commun. 8 (2017) 14390, https://doi.org/10.1038/ncomms14390.
[20] Z. Li, S. Zhao, R.O. Ritchie, M.A. Meyers, Mechanical properties of high-entropy alloys with emphasis on face-centered cubic alloys, Prog. Mater. Sci. 102 (2019) 296–345, https://doi.org/10.1016/j.pmatsci.2018.12.003.
[21] M. Rhode, T. Richter, D. Schroepfer, A.M. Manzoni, M. Schneider, G. Laplanche, Welding of high-entropy alloys and compositionally complex alloys—an overview, Weld. World 65 (2021) 1645–1659, https://doi.org/10.1007/s40194-021-01110-6.
[22] X. Meng, Y. Huang, J. Cao, J. Shen, J.F. dos Santos, Recent progress on control strategies for inherent issues in friction stir welding, Prog. Mater. Sci. 115 (2021), 100706, https://doi.org/10.1016/j.pmatsci.2020.100706.
[23] R. Nandan, T. DebRoy, H.K.D.H. Bhadeshia, Recent advances in friction-stir welding – process, weldment structure and properties, Prog. Mater. Sci. 53 (2008) 980–1023, https://doi.org/10.1016/j.pmatsci.2008.05.001.
[24] C. Poletti, F. Krumphals, S. Mitsche, Z. Gao, Microstructural evolution of AA6082 with small aluminides under hot torsion and friction stir processing, 2013. https://doi.org/10.4028/www.scientific.net/MSF.753.263.
[25] A. Simar, Y. Bréchet, B. de Meester, A. Denquin, T. Pardoen, Microstructure, local and global mechanical properties of friction stir welds in aluminium alloy 6005A-T6, Mater. Sci. Eng. A 486 (2008) 85–95, https://doi.org/10.1016/j.msea.2007.08.041.
[26] Y.D. Chung, H. Fujii, R. Ueji, N. Tsuji, Friction stir welding of high carbon steel with excellent toughness and ductility, Scr. Mater. 63 (2010) 223–226, https://doi.org/10.1016/j.scriptamat.2010.03.060.
[27] H. Fujii, R. Ueji, Y. Morisada, H. Tanigawa, High strength and ductility of friction-stir-welded steel joints due to mechanically stabilized metastable austenite, Scr. Mater. 70 (2014) 39–42, https://doi.org/10.1016/j.scriptamat.2013.09.012.
[28] Y. Hu, Y. Niu, Y. Zhao, W. Yang, X. Ma, J. Li, Friction stir welding of CoCrNi medium-entropy alloy: recrystallization behaviour and strengthening mechanism, Mater. Sci. Eng. A 848 (2022), 143361, https://doi.org/10.1016/j.msea.2022.143361.
[29] X. Qin, Y. Xu, Y. Sun, H. Fujii, Z. Zhu, C.H. Shek, Effect of process parameters on microstructure and mechanical properties of friction stir welded CoCrFeNi high entropy alloy, Mater. Sci. Eng. A 782 (2020), 139277, https://doi.org/10.1016/j.msea.2020.139277.
[30] N. Xu, Q. Song, Y. Bao, Microstructure evolution and mechanical properties of friction stir welded FeCrNiCoMn high-entropy alloy, Mater. Sci. Technol. 35 (2019) 577–584, https://doi.org/10.1080/02670836.2019.1573525.
[31] D. Shaysultanov, N. Stepanov, S. Malopheyev, I. Vysotskiy, V. Sanin, S. Mironov, R. Kaibyshev, G. Salishchev, S. Zherebtsov, Friction stir welding of a carbon-doped CoCrFeNiMn high-entropy alloy, Mater. Charact. 145 (2018) 353–361, https://doi.org/10.1016/j.matchar.2018.08.063.
[32] F. Xiong, R. Fu, Y. Li, D. Sang, Effects of nitrogen alloying and friction stir processing on the microstructures and mechanical properties of CoCrFeMnNi high-entropy alloys, J. Alloy. Compd. 822 (2020), 153512, https://doi.org/10.1016/j.jallcom.2019.153512.
[33] S. Park, H. Nam, Y. Na, H. Kim, Y. Moon, N. Kang, Effect of initial grain size on friction stir weldability for rolled and cast CoCrFeMnNi high-entropy alloys, Met. Mater. Int. 26 (2020) 641–649, https://doi.org/10.1007/s12540-019-00466-1.

[34] S. Park, H. Nam, J. Park, Y. Na, H. Kim, N. Kang, Superior-tensile property of CoCrFeMnNi alloys achieved using friction-stir welding for cryogenic applications, Mater. Sci. Eng. A 788 (2020), 139547, https://doi.org/10.1016/j.msea.2020.139547.

[35] M.-G. Jo, H.-J. Kim, M. Kang, P.P. Madakashira, E.S. Park, J.-Y. Suh, D.-I. Kim, S.-T. Hong, H.N. Han, Microstructure and mechanical properties of friction stir welded and laser welded high entropy alloy CrMnFeCoNi, Met. Mater. Int. 24 (2018) 73–83, https://doi.org/10.1007/s12540-017-7248-x.

[36] Z.G. Zhu, Y.F. Sun, M.H. Goh, F.L. Ng, Q.B. Nguyen, H. Fujii, S.M.L. Nai, J. Wei, C. H. Shek, Friction stir welding of a CoCrFeNiAl0.3 high entropy alloy, Mater. Lett. 205 (2017) 142–144, https://doi.org/10.1016/j.matlet.2017.06.073.

[37] N. Kumar, M. Komarasamy, P. Nelaturu, Z. Tang, P.K. Liaw, R.S. Mishra, Friction stir processing of a high entropy alloy Al0.1CoCrFeNi, JOM 67 (2015) 1007–1013, https://doi.org/10.1007/s11837-015-1385-9.

[38] Z.G. Zhu, Y.F. Sun, F.L. Ng, M.H. Goh, P.K. Liaw, H. Fujii, Q.B. Nguyen, Y. Xu, C. H. Shek, S.M.L. Nai, J. Wei, Friction-stir welding of a ductile high entropy alloy: microstructural evolution and weld strength, Mater. Sci. Eng. A 711 (2018) 524–532, https://doi.org/10.1016/j.msea.2017.11.058.

[39] P.-T. Lin, H.-C. Liu, P.-Y. Hsieh, C.-Y. Wei, C.-W. Tsai, Y.S. Sato, S.-C. Chen, H.-W. Yen, N.-H. Lu, C.-H. Chen, Heterogeneous structure-induced strength-ductility synergy by partial recrystallization during friction stir welding of a high-entropy alloy, Mater. Des. 197 (2021), 109238, https://doi.org/10.1016/j.matdes.2020.109238.

[40] S. Gupta, P. Agrawal, S.S. Nene, R.S. Mishra, Friction stir welding of γ-fcc dominated metastable high entropy alloy: microstructural evolution and strength, Scr. Mater. 204 (2021), 114161, https://doi.org/10.1016/j.scriptamat.2021.114161.

[41] H. Moghanni, K. Dehghani, A. Shafiei, Effects of process parameters on microstructure and mechanical properties of Al0.5CoCrFeNi high entropy alloy thin sheets using pinless friction stir welding, J. Mater. Res. Technol. 16 (2022) 1069–1089, https://doi.org/10.1016/j.jmrt.2021.12.050.

[42] T. Wang, S. Shukla, M. Komarasamy, K. Liu, R.S. Mishra, Towards heterogeneous AlxCoCrFeNi high entropy alloy via friction stir processing, Mater. Lett. 236 (2019) 472–475, https://doi.org/10.1016/j.matlet.2018.10.161.

[43] T. Wang, M. Komarasamy, S. Shukla, R.S. Mishra, Simultaneous enhancement of strength and ductility in an AlCoCrFeNi2.1 eutectic high-entropy alloy via friction stir processing, J. Alloy. Compd. 766 (2018) 312–317, https://doi.org/10.1016/j.jallcom.2018.06.337.

[44] S. Shashi Kumar, N. Murugan, K.K. Ramachandran, Influence of tool material on mechanical and microstructural properties of friction stir welded 316L austenitic stainless steel butt joints, Int. J. Refract. Met. Hard Mater. 58 (2016) 196–205, https://doi.org/10.1016/j.ijrmhm.2016.04.015.

[45] R. Ramesh, I. Dinaharan, R. Kumar, E.T. Akinlabi, Microstructure and mechanical characterization of friction-stir-welded 316L austenitic stainless steels, J. Mater. Eng. Perform. 28 (2019) 498–511, https://doi.org/10.1007/s11665-018-3802-z.

[46] S.S. Kumar, N. Murugan, K.K. Ramachandran, Effect of tool tilt angle on weld joint properties of friction stir welded AISI 316L stainless steel sheets, Measurement 150 (2020), 107083, https://doi.org/10.1016/j.measurement.2019.107083.

[47] S.S. Kumar, N. Murugan, K.K. Ramachandran, Microstructure and mechanical properties of friction stir welded AISI 316L austenitic stainless steel joints, J. Mater. Process. Technol. 254 (2018) 79–90, https://doi.org/10.1016/j.jmatprotec.2017.11.015.

[48] M. Hajian, A. Abdollah-zadeh, S.S. Rezaei-Nejad, H. Assadi, S.M.M. Hadavi, K. Chung, M. Shokouhimehr, Microstructure and mechanical properties of friction stir processed AISI 316L stainless steel, Mater. Des. 67 (2015) 82–94, https://doi.org/10.1016/j.matdes.2014.10.082.

[49] A.P. Reynolds, W. Tang, T. Gnaupel-Herold, H. Prask, Structure, properties, and residual stress of 304L stainless steel friction stir welds, Scr. Mater. 48 (2003) 1289–1294, https://doi.org/10.1016/S1359-6462(03)00024-1.

[50] S.H.C. Park, Y.S. Sato, H. Kokawa, K. Okamoto, S. Hirano, M. Inagaki, Rapid formation of the sigma phase in 304 stainless steel during friction stir welding, Scr. Mater. 49 (2003) 1175–1180, https://doi.org/10.1016/j.scriptamat.2003.08.022.

[51] H. Kokawa, S.H.C. Park, Y.S. Sato, K. Okamoto, S. Hirano, M. Inagaki, Microstructures in friction stir welded 304 austenitic stainless steel, Weld. World 49 (2005) 34–40, https://doi.org/10.1007/BF03266473.

[52] M.P. Meshram, R.R. Tamboli, B.K. Kodli, S.G. Yebaji, S.R. Dey, Texture analyses of friction stir welded austenitic stainless steel AISI-316L, Adv. Mater. Process. Technol. 4 (2018) 244–254, https://doi.org/10.1080/2374068X.2017.1414558.

[53] M. Nezakat, H. Akhiani, M. Hoseini, J. Szpunar, Effect of thermo-mechanical processing on texture evolution in austenitic stainless steel 316L, Mater. Charact. 98 (2014) 10–17, https://doi.org/10.1016/j.matchar.2014.10.006.

[54] J.-H. Cho, D.E. Boyce, P.R. Dawson, Modeling strain hardening and texture evolution in friction stir welding of stainless steel, Mater. Sci. Eng. A 398 (2005) 146–163, https://doi.org/10.1016/j.msea.2005.03.002.

[55] A. Dehghan-Manshadi, M.R. Barnett, P.D. Hodgson, Recrystallization in AISI 304 austenitic stainless steel during and after hot deformation, Mater. Sci. Eng. A 485 (2008) 664–672, https://doi.org/10.1016/j.msea.2007.08.026.

[56] D. Jorge-Badiola, A. Iza-Mendia, I. Gutiérrez, Study by EBSD of the development of the substructure in a hot deformed 304 stainless steel, Mater. Sci. Eng. A 394 (2005) 445–454, https://doi.org/10.1016/j.msea.2004.11.049.

[57] M. Schneider, E.P. George, T.J. Manescau, T. Záležák, J. Hunfeld, A. Dlouhý, G. Eggeler, G. Laplanche, Analysis of strengthening due to grain boundaries and annealing twin boundaries in the CrCoNi medium-entropy alloy, Int. J. Plast. 124 (2020) 155–169, https://doi.org/10.1016/j.ijplas.2019.08.009.

[58] G. Laplanche, A. Kostka, C. Reinhart, J. Hunfeld, G. Eggeler, E.P. George, Reasons for the superior mechanical properties of medium-entropy CrCoNi compared to high-entropy CrMnFeCoNi, Acta Mater. 128 (2017) 292–303, https://doi.org/10.1016/j.actamat.2017.02.036.

[59] C. Stephan-Scherb, W. Schulz, M. Schneider, S. Karafiludis, G. Laplanche, High-temperature oxidation in dry and humid atmospheres of the equiatomic CrMnFeCoNi and CrCoNi high- and medium-entropy alloys, Oxid. Met. 95 (2021) 105–133, https://doi.org/10.1007/s11085-020-10014-7.

[60] T. Richter, D. Schroepfer, M. Rhode, Residual stresses in a high- and a medium-entropy alloy due to TIG and friction stir welding, J. Manuf. Mater. Process 6 (2022), https://doi.org/10.3390/jmmp6060147.

[61] N. Xu, R. Ueji, H. Fujii, Dynamic and static change of grain size and texture of copper during friction stir welding, J. Mater. Process. Technol. 232 (2016) 90–99, https://doi.org/10.1016/j.jmatprotec.2016.01.021.

[62] S.H.C. Park, Y.S. Sato, H. Kokawa, K. Okamoto, S. Hirano, M. Inagaki, Microstructural characterisation of stir zone containing residual ferrite in friction stir welded 304 austenitic stainless steel, Sci. Technol. Weld. Join. 10 (2005) 550–556, https://doi.org/10.1179/174329305×46691.

[63] S. Shashi Kumar, N. Murugan, K.K. Ramachandran, Effect of friction stir welding on mechanical and microstructural properties of AISI 316L stainless steel butt joints, Weld. World 63 (2019) 137–150, https://doi.org/10.1007/s40194-018-0621-7.

[64] H. Gao, Y. Huang, Geometrically necessary dislocation and size-dependent plasticity, Scr. Mater. 48 (2003) 113–118, https://doi.org/10.1016/S1359-6462(02)00329-9.

[65] R.S. Mishra, Z.Y. Ma, Friction stir welding and processing, Mater. Sci. Eng. R. Rep. 50 (2005) 1–78, https://doi.org/10.1016/j.mser.2005.07.001.

[66] D.G. Andrade, C. Leitão, N. Dialami, M. Chiumenti, D.M. Rodrigues, Analysis of contact conditions and its influence on strain rate and temperature in friction stir welding, Int. J. Mech. Sci. 191 (2021), 106095, https://doi.org/10.1016/j.ijmecsci.2020.106095.

[67] K. Easterling, Chapter3 - The heat-affected zone, in: K. Easterling (Ed.), Introd. to Phys. Metall. Weld. (Second Ed., Second Edi, Butterworth-Heinemann, 1992: pp. 126–190. https://doi.org/https://doi.org/10.1016/B978–0-7506–0394-2.50008–3.

[68] L.E. Murr, Some observations of grain boundary ledges and ledges as dislocation sources in metals and alloys, Metall. Trans. A 6 (1975) 505, https://doi.org/10.1007/BF02658408.

[69] E.V. Esquivel, L.E. Murr, Grain boundary contributions to deformation and solid-state flow in severe plastic deformation, Mater. Sci. Eng. A 409 (2005) 13–23, https://doi.org/10.1016/j.msea.2005.04.063.

[70] L.E. Murr, Strain-induced dislocation emission from grain boundaries in stainless steel, Mater. Sci. Eng. 51 (1981) 71–79, https://doi.org/10.1016/0025-5416(81)90108-7.

[71] K. Huang, R.E. Logé, A review of dynamic recrystallization phenomena in metallic materials, Mater. Des. 111 (2016) 548–574, https://doi.org/10.1016/j.matdes.2016.09.012.

[72] F.J. Humphreys, M. Hatherly, Recrystallization and related annealing phenomena, Elsevier,, 2004. ⟨http://www.sciencedirect.com/science/book/9780080441641⟩. accessed June 7, 2017.

[73] S.F. Liu, Y. Wu, H.T. Wang, J.Y. He, J.B. Liu, C.X. Chen, X.J. Liu, H. Wang, Z.P. Lu, Stacking fault energy of face-centered-cubic high entropy alloys, Intermetallics 93 (2018) 269–273, https://doi.org/10.1016/j.intermet.2017.10.004.

[74] S. Huang, W. Li, S. Lu, F. Tian, J. Shen, E. Holmström, L. Vitos, Temperature dependent stacking fault energy of FeCrCoNiMn high entropy alloy, Scr. Mater. 108 (2015) 44–47, https://doi.org/10.1016/j.scriptamat.2015.05.041.

[75] T.Z. Khan, T. Kirk, G. Vazquez, P. Singh, A.V. Smirnov, D.D. Johnson, K. Youssef, R. Arróyave, Towards stacking fault energy engineering in FCC high entropy alloys, Acta Mater. 224 (2022), 117472, https://doi.org/10.1016/j.actamat.2021.117472.

[76] F. Montheillet, J. Le Coze, Influence of purity on the dynamic recrystallization of metals and alloys, Phys. Status Solidi 189 (2002) 51–58, https://doi.org/https://doi.org/10.1002/1521-396X(200201)189:1<51::AID-PSSA51>3.0.CO;2-M.

[77] X. Wang, D. Wang, J. Jin, J. Li, Effects of strain rates and twins evolution on dynamic recrystallization mechanisms of austenite stainless steel, Mater. Sci. Eng. A 761 (2019), 138044, https://doi.org/10.1016/j.msea.2019.138044.

[78] T. Sakai, A. Belyakov, R. Kaibyshev, H. Miura, J.J. Jonas, Dynamic and post-dynamic recrystallization under hot, cold and severe plastic deformation conditions, Prog. Mater. Sci. 60 (2014) 130–207, https://doi.org/10.1016/j.pmatsci.2013.09.002.

[79] G. Laplanche, M. Schneider, F. Scholz, J. Frenzel, G. Eggeler, J. Schreuer, Processing of a single-crystalline CrCoNi medium-entropy alloy and evolution of its thermal expansion and elastic stiffness coefficients with temperature, Scr. Mater. 177 (2020) 44–48, https://doi.org/10.1016/j.scriptamat.2019.09.020.

[80] Z. Wu, H. Bei, G.M. Pharr, E.P. George, Temperature dependence of the mechanical properties of equiatomic solid solution alloys with face-centered cubic crystal structures, Acta Mater. 81 (2014) 428–441, https://doi.org/10.1016/j.actamat.2014.08.026.

[81] A.V. Korchuganov, I.S. Lutsenko, Molecular dynamics research of mechanical, diffusion and thermal properties of CoCrFeMnNi high-entropy alloys, AIP Conf. Proc. 2053 (2018) 40046, https://doi.org/10.1063/1.5084484.

[82] K. Arun Babu, C.N. Athreya, Y.H. Mozumder, V. Subramanya Sarma, S. Mandal, A comprehensive study on texture development and twin-related domain evolution following hot compression in a super austenitic stainless steel, Metall. Mater. Trans. A 51 (2020) 3535–3551, https://doi.org/10.1007/s11661-020-05763-8.